https://doi.org/10.5194/egusphere-2026-2182
Preprint. Discussion started: 19 May 2026

First observations of aerosol mass fluxes over open water using a large-aperture scintillometer

Renjie Liu[1], Yuhong Pu[1], Renmin Yuan[2], Chaoxun Hang[1*]

[1]School of Oceanography, Shanghai Jiao Tong University, Shanghai 200030, PR China
[2]School of Earth and Space Sciences, University of Science and Technology of China, Hefei 230026, PR China

Correspondence to: Chaoxun Hang (hangchaoxun@sjtu.edu.cn)

Abstract. Near-surface aerosol fluxes over open water are critical for understanding air–sea interactions and atmospheric radiative budgets, yet direct micrometeorological observations remain very limited. To address this gap, this study presents the first application of a large-aperture scintillometer (LAS) for retrieving aerosol mass fluxes over open-water environments, including an inland lake and a coastal bay. LAS-derived fluxes were compared with conventional eddy-covariance (EC) measurements and independent dry-deposition calculations. Under conditions without severe optical attenuation, the LAS-derived fluxes exhibited temporal variations broadly consistent with EC measurements, with normalized root-mean-square errors (NRMSEs) to 15.0%–16.8%. The coastal campaigns revealed the operational boundary of this optical approach: dense fog and persistent high humidity severely attenuated the LAS signal and caused extended data gaps. Comparisons with dry-deposition calculations further showed that the path-averaged LAS measurements may better capture site-scale variability at the coastal site. Overall, these results demonstrate the potential of LAS as a valuable complements to traditional point measurements for characterizing aerosol exchange over open water.

1 Introdution

Aerosols influence climate and boundary-layer processes through their roles in radiation, cloud microphysics, and vertical exchange. Acting as cloud condensation nuclei, they modify droplet number concentration and size and affect cloud albedo and precipitation development (Sasakawa et al., 2003; Seinfeld et al., 2016). By scattering and absorbing solar radiation, aerosols also perturb surface energy balance (Twomey, 1977). In particular, absorbing aerosols can heat the air aloft (Huang et al., 2018), stabilize the lower troposphere, suppress turbulent mixing, and reduce boundary-layer depth (Ding et al., 2016), thereby feeding back on the accumulation and transport of particles near the surface (Li et al., 2021).

The ocean covers about 71% of the Earth's surface and is a major natural source of atmospheric aerosols (Kiehl and Briegleb., 1993). Marine aerosol populations are dominated by sea salt, with additional contributions from marine organic matter and secondary aerosol formed from ocean-emitted precursor gases. Owing to their high hygroscopicity, marine particles efficiently act as cloud condensation nuclei, and influence sea fog, low clouds, and radiative transfer (Sasakawa et al., 2003; Gaston et al., 2018). Sea-salt particles also participate in heterogeneous halogen chemistry (Lewis and Schwartz,

https://doi.org/10.5194/egusphere-2026-2182
Preprint. Discussion started: 19 May 2026

2004; Hsu et al., 2007; Laskin et al., 2012), while marine sulfur emissions such as dimethyl sulfide (DMS) contribute indirectly to sulfate aerosol formation, with an annual flux exceeding 2.8×10^7 t (Lana et al., 2011). Collectively, these processes make aerosol exchange across the air-sea interface an important component of marine boundary layer chemistry and climate.

Most previous marine aerosol studies have focused on concentration, chemical composition, or optical properties measured with filter sampling, beta-attenuation methods, scanning mobility particle sizers, and optical particle counters. In contrast, direct observations of aerosol fluxes, particularly mass fluxes across the air–sea interface, remain scarce. Existing constraints are derived predominantly from terrestrial, coastal, or short-duration campaigns, leaving the open-water surface layer insufficiently sampled. This observational gap limits the evaluation of air–sea exchange parameterizations and aerosol–cloud–radiation interactions in marine environments (Revell et al., 2019; Huang and Ding, 2021).

Over the ocean, the net vertical aerosol mass flux reflects the combined effects of sea-spray production, deposition, transport, and local processing. For coarse-mode marine aerosol, upward production by wave breaking and bubble bursting is often the dominant source term, but the measured net flux at a given height also includes downward deposition and advective influences (Monahan et al., 1986; Andreas, 1998; 2002). Widely used whitecap-based source functions parameterize sea-spray emission mainly as a function of 10-m wind speed (Monahan et al., 1986; Gong, 2003; Ovadnevaite et al., 2014; Salter et al., 2015). These schemes are convenient for estimating source strength, but they do not directly provide observed net mass fluxes, and their uncertainty can remain large because sea state, humidity, and aerosol composition are only partly represented (De Leeuw et al., 2011; Fuentes et al., 2010; Hultin et al., 2010; Zábori et al., 2013).

The eddy-covariance (EC) technique provides a direct micrometeorological framework for measuring aerosol exchange by correlating turbulent vertical velocity with aerosol fluctuations (Geever et al., 2005; Norris et al., 2008; Yang et al., 2016; Zinke et al., 2024). However, most marine EC studies emphasize number fluxes because fast-response particle counters are more readily available than direct mass measurements. Converting number flux to mass flux requires additional assumptions about particle size distributions, density, shape, and hygroscopic growth, all of which can vary strongly over water. Direct observations of aerosol mass fluxes over open water therefore remain very limited.

Large Aperture Scintillometers (LAS) offer path-integrated measurements over hundreds of meters to kilometers and are attractive for heterogeneous surfaces where single-point measurements may not be regionally representative (Chehbouni et al., 1999; Ward et al., 2014). Previous studies have shown that LAS can be used to infer aerosol mass fluxes over land from the high- and low-frequency components of optical scintillation, and recent work reported broad agreement with EC for temporal trends and diurnal cycles over terrestrial surfaces (Yuan et al., 2016; 2019; 2024). Whether this approach remains valid over open water is still unknown. Marine conditions introduce additional challenges, high humidity and fog-induced beam attenuation, hygroscopic growth of sea-salt particles, and difference in spatial representativeness between path-averaged and point measurements.

To address this gap, we conducted four open-water field campaigns over an inland lake and a coastal marine site. We applied the LAS method to retrieve aerosol mass fluxes over water and compared the results with concurrent EC measurements and

https://doi.org/10.5194/egusphere-2026-2182
Preprint. Discussion started: 19 May 2026

aerosol particle sampling. Our goal is to evaluate the feasibility of LAS-based aerosol mass flux retrieval over open water and to identify the conditions under which it can provide useful measurements. Rather than treating the EC system as a strict truth standard, we used the LAS-EC comparison to assess consistency in temporal variability and to examine how footprint differences affect agreement between two methods. We further compared both micrometeorological estimates with filter-based dry-deposition calculations as an additional, non-equivalent observational constraint.

2 Observation setup and methods

2.1 Study site and observation configuration

A total of four field campaigns were conducted at two open-water sites in eastern China: Siyuan Lake at Shanghai Jiao Tong University, Shanghai (31°01′15″ N, 121°25′48″ E), and a coastal bay site on Sijiao Island in the Shengsi Archipelago, Zhejiang Province (30°42′15″ N, 122°31′10″ E). Two campaigns were conducted at each site. Continuous LAS and EC observations were performed during each campaign, together with intermittent filter-based aerosol sampling.

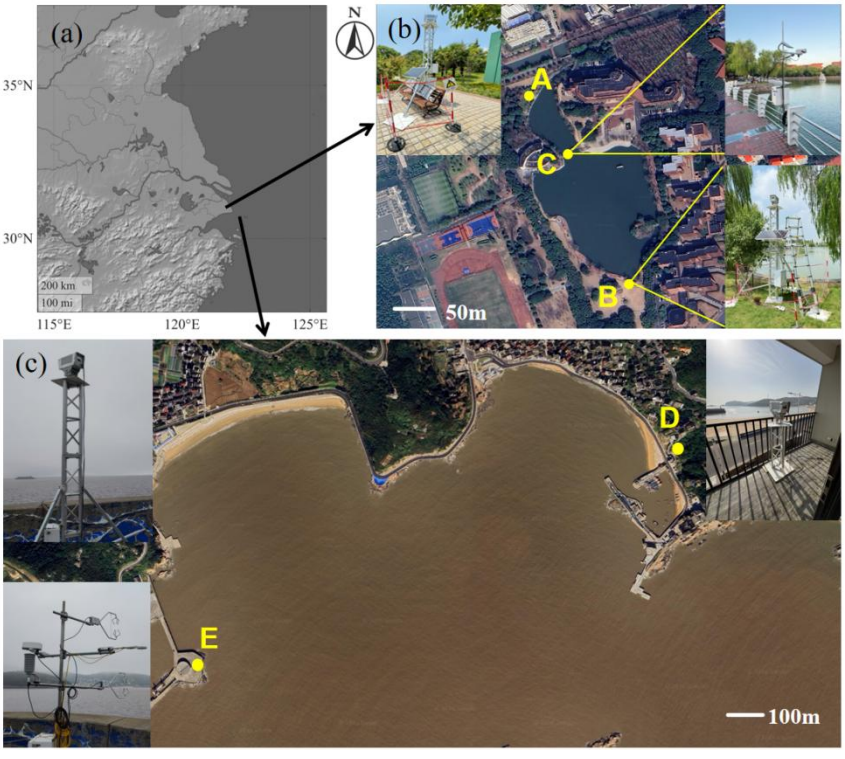

Figure 1. (a) Map of eastern China showing the locations of the two study sites; **(b)** Siyuan Lake site. Points A and B are the transmitter and receiver of the large aperture scintillometer (LAS), respectively; C is the eddy covariance (EC) system. **(c)** The study site of Sijiao Island. Point D is the transmitter of LAS, and E denotes both the LAS receiver and the EC system. Inset photographs display the actual site layout. Map data in **(a)** © 2026 Google; satellite imagery in **(b)** and **(c)** © 2026 Google Earth.

https://doi.org/10.5194/egusphere-2026-2182
Preprint. Discussion started: 19 May 2026

The first site, Siyuan Lake, is located on the Shanghai Jiao Tong University campus in an urban environment. As shown in Fig. 1b, The LAS transmitter was installed on the southern side of the lake (point A), and the receiver was located on the northern side (point B), yielding a path length of 290 m. The transmitter and receiver were mounted on 3 m towers, giving effective path heights of 4.35 m and 4.65 m above the water surface during the first and second campaigns, respectively. The LAS system (Aiutyl-LAS, Sciencesky) has an aperture diameter of 0.15 m and operates at a wavelength of 625 nm, and records data at a sampling frequency of 500 Hz. A co-located EC system was installed on a bridge over the lake (point C), mounted at heights of 3.85 m and 4.15 m above the water surface during the first and second campaigns, respectively. The system consisted of a 3-D sonic anemometer (CSAT3B, Campbell Scientific) sampling at 20 Hz, along with a visibility sensor (PWD50, Vaisala), a temperature-humidity sensor (HMP155A, Vaisala) and a barometric pressure sensor (CS106, Vaisala), all recording at 1 Hz. The two campaigns at this site were conducted from 11 August to 17 September 2024, and from 26 December 2024 to 28 February 2025.

The second site was located at a coastal bay on the eastern side of Sijiao Island in the East China Sea. Natural vegetation dominates the eastern part of the island, whereas urbanized areas are concentrated in the west. As shown in Fig. 1c, the LAS transmitter was installed on the eastern side of the bay (point D), while the LAS receiver and the EC system were located on the western side (point E). The LAS path length was 1300 m, and the effective path height was 6.5 m above the sea surface. The EC system was mounted at a height of 6.13 m, with its instruments and supporting meteorological configured identically to those described above to ensure the comparability of the different datasets at Siyuan Lake. This site is far from the main urbanized area of the island and is therefore less directly affected by local traffic emissions. The two campaigns at this site were conducted from 16 to 21 April 2025 and from 30 August to 4 September 2025.

2.2 Data processing and quality control

All observational data were subjected to a unified quality-control procedure before flux calculation. The primary variables included air temperature, wind speed, visibility, relative humidity, barometric pressure, and the LAS optical signal.

Spikes were identified using a ±3 standard deviation criterion relative to a 2 h moving average. Any data point deviating by more than three standard deviations from this moving average was flagged as a spike and replaced with NaN. Additional filtering was applied to the LAS data. Periods with precipitation (rainfall rates ≥ 0.1 mm h^{-1}), persistent heavy fog causing signal loss or unstable operation, and intervals without clear spectrum separation in the log-intensity signal were discarded. For the EC calculations, wind directions within ±20° of the supporting tower were excluded to reduce flow distortion. A 30 min averaging period was adopted for EC flux calculations to retain the turbulent contribution while filtering out low-frequency motions. The rationale of this averaging period is provided in Appendix A. After all quality-control procedures were applied, 70.8% of the original observations were retained for the Siyuan Lake campaigns and 80.5% for the Sijiao Island campaigns.

https://doi.org/10.5194/egusphere-2026-2182
Preprint. Discussion started: 19 May 2026

2.3 LAS-based retrieval of aerosol mass flux

LAS obtains the atmospheric equivalent refractive index structure parameter (C_n^2) by measuring fluctuations in light intensity along an optical path. According to complex refractive index theory (van de Hulst, 1957; Yuan et al., 2021), the atmospheric equivalent refractive index n consists of a real component (n_{Re}) and an imaginary component (n_{Im}). The n_{Re} is sensitive to temperature, and the n_{Im} is sensitive to the concentration of light-absorbing aerosols. Accordingly, the C_n^2 also comprises a real part ($C_{n,Re}^2$) and an imaginary part ($C_{n,Im}^2$). The temporal spectrum of the log-intensity obtained from LAS can be decomposed into high-frequency and low-frequency components (Yuan et al., 2024). The high-frequency variance ($\sigma_{lnI,Re}^2$) is caused by the real part of the structure parameter, whereas the low-frequency variance ($\sigma_{lnI,Im}^2$) is due to the imaginary part. The $C_{n,Re}^2$ and $C_{n,Im}^2$ can be derived from these variances as follows (Yuan et al., 2015):

$$C_{n,Re}^2 = 1.12\,\sigma_{lnI,Re}^2\,L^{-3}\,D_t^{7/6}\,D_r^{7/6}\,, \tag{1}$$

$$C_{n,Im}^2 = 0.34\sigma_{lnI,Im}^2\,\eta^{-2}\,L_0^{-5/3}\,L^{-1}\,, \tag{2}$$

where $\sigma_{lnI,Re}^2$ and $\sigma_{lnI,Im}^2$ represent the variances at the high-frequency and low-frequency ends, respectively; L is the path length; D_t and D_r are the transmitter and receiver aperture diameters, respectively; L_0 is the outer scale of turbulence; η is the optical wavenumber. $C_{n,Re}^2$ and $C_{n,Im}^2$ are the structure parameters for the real and imaginary parts of the atmospheric equivalent refractive index, respectively.

To relate these optical structure parameters to the aerosol mass flux, two conversion factors are required. R_{TN} represents the ratio of the equivalent real refractive index change to temperature fluctuations, and R_{MN} relates the imaginary refractive index to the aerosol mass concentration (Tatarskii, 1961; Yuan et al., 2021):

$$R_{TN} = 1.29\times10^4\times\left(1+\frac{7.52\times10^{-3}}{\lambda^2}\right)^{-1}\frac{\overline{T}^2}{\overline{P}}\,, \tag{3}$$

$$R_{MN} = \frac{4\pi\,M_a}{\lambda\,\beta_{ext}}\,, \tag{4}$$

where λ is the light wavelength; P is atmospheric pressure; T is temperature; M_a is aerosol mass concentration approximated as PM_{10}; β_{ext} is the extinction coefficient, inversely proportional to visibility $visib$ ($\beta_{ext} = \frac{3.912}{visib}$).

Based on these optical and meteorological relationships, the aerosol mass flux can be calculated as follows (Yuan et al., 2024):

$$F_{a\_LAS} = a\,(\tfrac{g}{T})^{1/2}\,R_{TN}^{1/2}\,(C_{n,Re}^2)^{1/4}\,R_{MN}\,(C_{n,Im}^2)^{1/2}\,(z-d)\,, \tag{5}$$

where $a = 0.567$ (De Bruin et al., 1995); g is gravitational acceleration; z is instrument mounting height; d is zero-plane displacement.

https://doi.org/10.5194/egusphere-2026-2182
Preprint. Discussion started: 19 May 2026

2.4 EC-based estimation of aerosol mass flux

The EC method is a commonly used technique for quantifying turbulent exchange fluxes in the atmospheric surface layer. It estimates the aerosol mass flux by calculating the covariance between high-frequency vertical wind velocity fluctuations and extinction coefficient fluctuations. The aerosol mass flux can be calculated by EC method as follows (Wilczak et al., 2001):

$$F_{a\_EC} = R_{MN} \frac{\lambda}{4\pi} \overline{w'\beta_{ext}'}, \quad (6)$$

where $\overline{w'\beta_{ext}'}$ is the covariance between vertical wind velocity w and extinction coefficient β_{ext}.

2.5 Filter-based aerosol sampling and dry-deposition calculation

To provide an independent methodological reference, filter-based aerosol sampling was conducted alongside the micrometeorological measurements. A medium-flow air sampler (TH-150H, Tianhong) operating at $100\ L\ min^{-1}$ was deployed to collect particles on glass fiber filters with $PM_{2.5}$ and PM_{10} impactors. Both before and after sampling, filters were equilibrated in a constant temperature environment ($45 \pm 1°C$) for 3 hours and weighed using an analytical balance (EAB 125i, Adam) with a precision of 0.1 mg. The mass of collected particulate matter was determined by the weight difference of the filter before and after sampling, allowing the calculation of particulate mass concentration as follows:

$$C_x = \frac{m_{2,x} - m_{1,x}}{V}, \quad (7)$$

where the subscript x denotes the specific size fraction (i.e., $PM_{2.5}$ or $PM_{2.5\ to\ 10}$); $m_{2,x}$ is the mass after sampling; $m_{1,x}$ is the mass before sampling; V is the sampling volume.

According to size-resolved deposition models (Slinn et al., 1978; Petroff and Zhang, 2010; Seinfeld and Pandis, 2016), the dry-deposition velocity (v_d) is parameterized using a traditional resistance framework:

$$v_d = v_s + \frac{1}{R_a + R_s}, \quad (8)$$

where v_s is the particle settling velocity; R_a is the aerodynamic resistance; R_s is the surface resistance, which includes Brownian diffusion and inertial impaction over water surfaces.

Based on this theoretical framework and the typical size characteristics of marine aerosols, the representative deposition velocities for $PM_{2.5}$ and $PM_{2.5\ to\ 10}$ were derived. With these deposition velocities and the mass concentrations determined above, the dry-deposition flux can be calculated as follows:

$$F_{a\_DD} = C_{PM_{2.5}} v_{PM_{2.5}} + C_{PM_{2.5-10}} v_{PM_{2.5\ to\ 10}}, \quad (9)$$

where $C_{PM_{2.5}}$ and $C_{PM_{2.5\ to\ 10}}$ are the mass concentrations of $PM_{2.5}$ and $PM_{2.5\ to\ 10}$ separated by the impactors, respectively; $v_{PM_{2.5}}$ and $v_{PM_{2.5\ to\ 10}}$ are the deposition velocities for $PM_{2.5}$ and $PM_{2.5\ to\ 10}$, respectively.

https://doi.org/10.5194/egusphere-2026-2182
Preprint. Discussion started: 19 May 2026

2.6 Footprint analysis for LAS and EC

For the single-point EC measurements, the footprint was determined using a two-dimensional footprint parameterization model (Kljun et al., 2015). This model calculates the relative contribution $f_{EC}(x,y)$ of each upwind surface pixel to the measured flux.

In contrast, LAS represents a path-averaged measurement. The footprint of the LAS can be determined by taking the product of the localized flux footprints along the optical path and the normalized spatial weighting function of the scintillometer (Meijninger et al., 2002; Hartogensis et al., 2003):

$$f_{LAS}(x, y, Z_m) = \int_{x_1}^{x_2} W(x) f(x - x', y - y', Z_m)\, \mathrm{d}x\,, \tag{10}$$

where $W(x)$ is the weighting function; x_1 and x_2 are the positions of transmitter and receiver of LAS, respectively; x and y are the points along the optical path; x' and y' are the points in the up-wind areas; Z_m is the effective height $(z - d)$; f is the flux footprint at a single point.

3 Results

3.1 Overview of meteorological conditions

To provide environmental context for the aerosol flux analysis, the main meteorological conditions during the four field campaigns are summarized in Table 1. At Siyuan Lake, the first campaign was characterized by weak wind speeds (mean 1.19 m s^{-1}), predominantly southeasterly flow (78%). warm condition (mean 31.8 °C), and RH ranging from 40% to 100%. Mean pressure was 1006.7 hPa; with a marked drop to 991.8 hPa during the typhoon passage on 16 September 2024. The second lake campaign was colder (mean 5.7 °C), similar weak wind (mean 0.96 m s^{-1}), and more strongly affected by synoptic winter high pressure, pressure increased to 1026.1 hPa; RH ranged from 20% to 100%. Several precipitation events occurred during both lake campaigns, and data affected by rainfall or the typhoon were excluded from the subsequent flux analysis.

At Sijiao Island, both campaigns were characterized by stronger winds than at Siyuan Lake (2.31 m s^{-1} and 2.07 m s^{-1}, respectively) and predominantly southerly flow (72% and 89%). The first and second coastal campaigns had mean air temperatures of 16.7 °C and 26.9 °C, respectively, with relatively small diurnal differences (~4 °C and ~2 °C). RH remained persistently high, especially in the second campaign (80% − 100%), while mean pressures remained relatively stable between the two campaigns. No rainfall occurred during either coastal campaign. However, dense fog (visib < 5000m) during 18 - 19 April 2025, and 00:00–02:00 LST on 21 April caused severe LAS signal attenuation and is therefore important for interpreting the first coastal campaign.

Table 1. Summary of the meteorological conditions during the four observational campaigns at Siyuan Lake and Sijiao Island.

https://doi.org/10.5194/egusphere-2026-2182
Preprint. Discussion started: 19 May 2026

Site	Siyuan Lake		Sijiao Island	
Observation Period	First (Aug – Sep 2024)	Second (Dec 2024 – Feb 2025)	First (Apr 2025)	Second (Aug – Sep 2025)
Mean T (°C)	31.8	5.7	16.7	26.9
Diurnal T Range (°C)	>7	>12	~ 4	~ 2
Mean WS (m s^{-1})	1.19	0.96	2.31	2.07
Prevailing WD (%)	SE (78%)	NW (51%)	S (72%)	S (89%)
RH Range (%)	40 – 100	20 – 100	60 – 100	80 – 100
Mean P (hPa)	1006.7	1026.1	1008.8	1008.5
Notable Weather Events	Typhoon (16 Sep 2024; 991.8 hPa); Rain (Aug 27 – 28, Sep 3, 10 – 11, 15 – 16)	Rain (Jan 26, 31 – Feb 1, Feb 11, 14 – 15, 27)	Fog (18 – 19 Apr 2025; 21 Apr 00:00 – 02:00 LST)	None

Note. T: air temperature; WS: wind speed; WD: wind direction; RH: relative humidity; P: atmospheric pressure. The diurnal T range represents the approximate maximum daily temperature difference.

3.2 Comparison of LAS and EC aerosol fluxes over Siyuan Lake

3.2.1 Temporal variations and footprint analysis over Siyuan Lake

Siyuan Lake provides a relatively simple inland open-water setting for the initial comparison between LAS and EC. Fig. 2 shows the temporal variations of aerosol fluxes derived from LAS and EC in the two Siyuan Lake campaigns. The background transparent points represent the original 30-min data, whereas the solid lines denote 2 h block averages used to emphasize broader temporal variability. At the block-averaged scale, LAS and EC show similar temporal evolution, with broadly coincident periods of increasing and decreasing flux. Both methods also resolve the seasonal contrast between the two observation campaigns, with higher fluxes in the warm season and lower fluxes in cold season. During the first campaign, the mean aerosol fluxes measured by LAS and EC are 0.127 μg m^{-2} s^{-1} and 0.086 μg m^{-2} s^{-1}, respectively, corresponding to a mean bias error (MBE) of 0.041 μg m^{-2} s^{-1}. During the second campaign, the mean fluxes decrease to 0.068 μg m^{-2} s^{-1} and 0.049 μg m^{-2} s^{-1}, with an MBE of 0.019 μg m^{-2} s^{-1}. In both lake campaigns, aerosol fluxes from LAS were larger than those obtained from EC, consistent with the terrestrial comparison reported by Yuan et al. (2024). Despite this systematic difference in magnitude, the normalized root-mean-square error (NRMSE) of the 2 h block averages remain

https://doi.org/10.5194/egusphere-2026-2182
Preprint. Discussion started: 19 May 2026

limited to 16.3% and 15.0% in the first and second lake campaigns, respectively, indicating reasonable agreement at the macroscopic timescale.

In contrast, the correlation between the original 30-min time series was weak ($r = 0.104$ and 0.301 for the first and second lake campaigns, respectively. This weak short-timescale correlation is consistent with differences in spatial representativeness between the two methods. As shown by the footprint analysis in Fig. 3, the relatively short LAS path over the lake yields a footprint scale comparable to that of the EC system, but the two source areas still do not fully overlap. The EC footprint is strongly modulated by local wind conditions and may extend asymmetrically, whereas the LAS footprint is weighted along the fixed optical path. Given the spatial heterogeneity of the site, this mismatch likely causes the two systems to sample different source areas at a given time, thereby reducing point-to-point agreement.

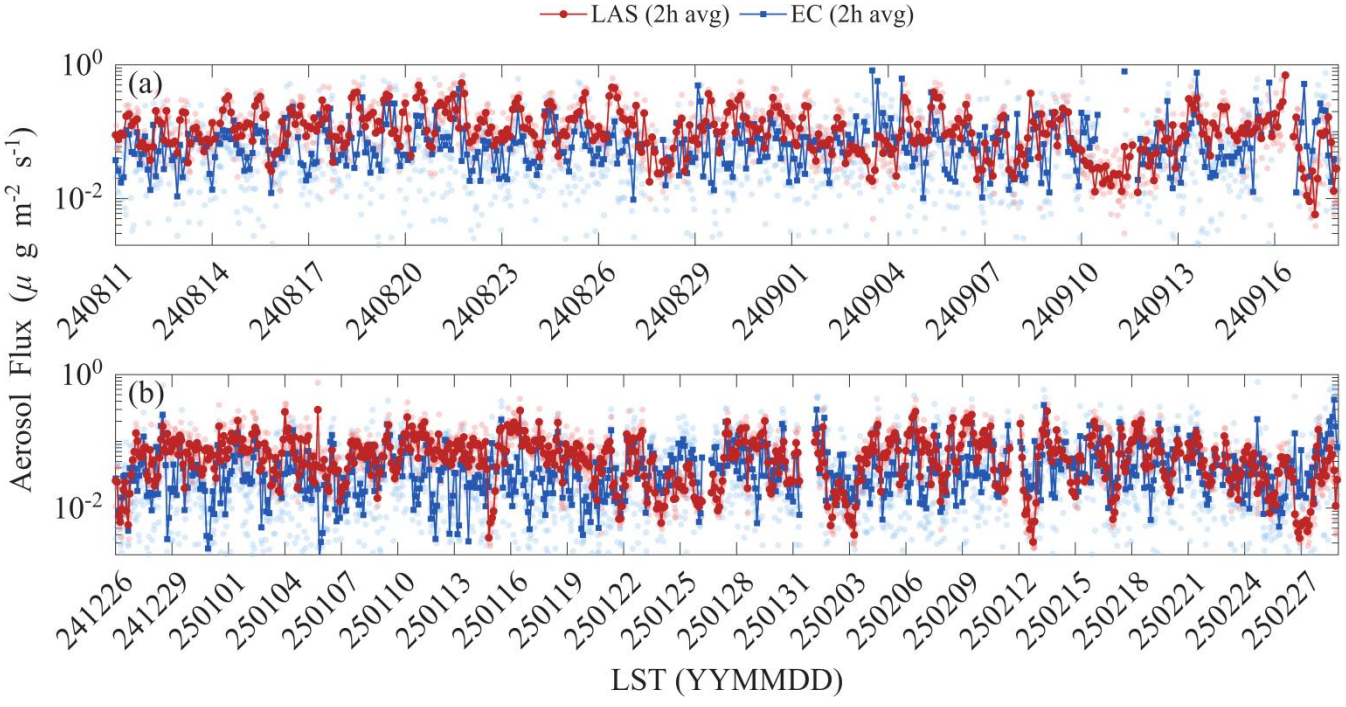

Figure 2. Temporal variations of aerosol fluxes derived from LAS and EC measurements in **(a)** the first campaign (11 August to 17 September 2024) and **(b)** the second campaign (26 December 2024 to 28 February 2025) at Siyuan Lake. The solid lines with red circles and blue squares denote the 2 h block averages for LAS and EC, respectively. The transparent points indicate the original data at a 30-min resolution.

https://doi.org/10.5194/egusphere-2026-2182
Preprint. Discussion started: 19 May 2026

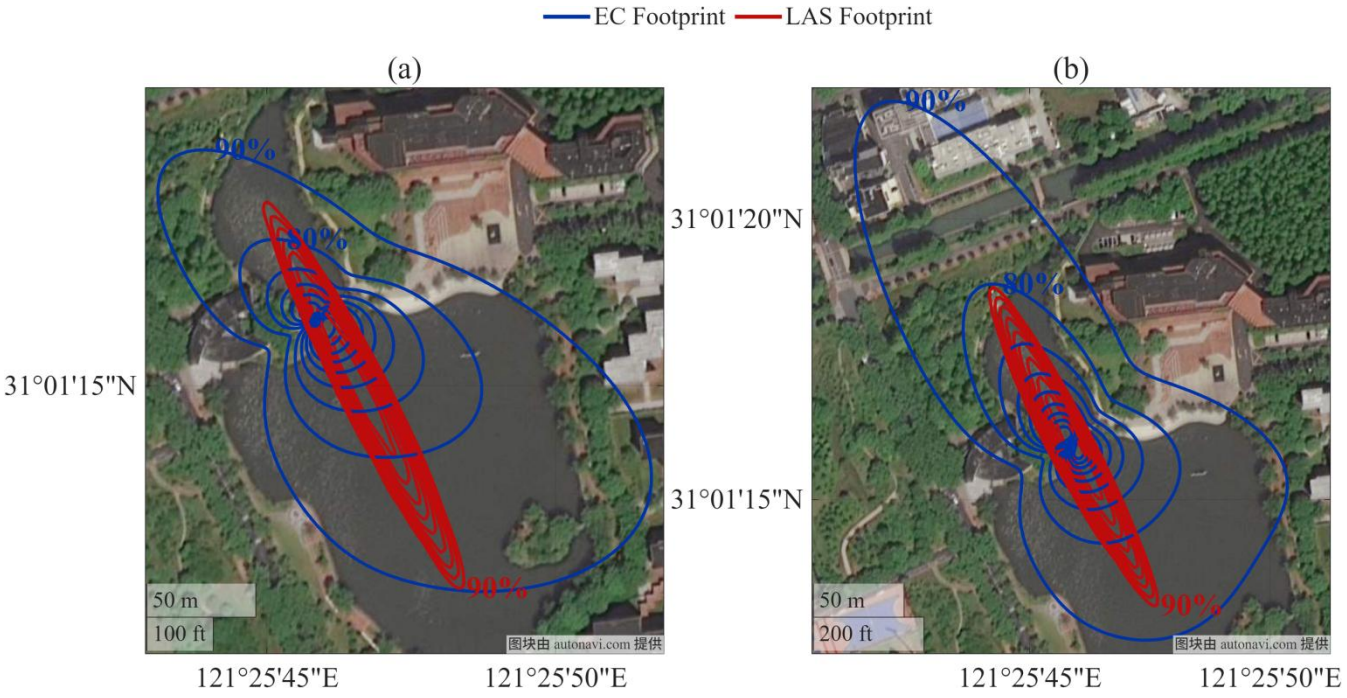

Figure 3. Spatial footprint climatology of the EC (blue solid lines) and LAS (red solid lines) systems over Siyuan Lake in **(a)** the first campaign and **(b)** the second campaign. The contour lines denote the cumulative spatial contribution to the measured aerosol fluxes, representing the 10% to 90% source areas from the inside out at 10% intervals. Map tiles provided by © 2026 AutoNavi.

3.2.2 Ensemble diurnal cycles of aerosol fluxes over Siyuan Lake

To investigate the diurnal behavior of aerosol fluxes, ensemble average cycles were conducted for both lake campaigns. As shown in Fig. 4, the ensemble diurnal cycles of LAS and EC are broadly synchronized. The correlation between the ensemble mean curves increases 0.645 and 0.656 in the first and second lake campaigns, respectively, indicating a consistent agreement between the two methods.

Both methods show higher fluxes during daytime and lower values at night, a pattern consistent with stronger daytime turbulent exchange over the lake. For the second lake campaign, the daytime peak fluxes were 0.145 $\mu g\ m^{-2}\ s^{-1}$ and 0.108 $\mu g\ m^{-2}\ s^{-1}$ for LAS and EC respectively, and both occurred at 12:30 LST. In the first lake campaign, the corresponding peak fluxes increase to 0.297 $\mu g\ m^{-2}\ s^{-1}$ and 0.223 $\mu g\ m^{-2}\ s^{-1}$. In contrast, the first campaign shows a difference in peak timing, with LAS peaking at 11:00 LST and EC peaking at 14:00 LST. This offset is consistent with the footprints mismatch discussed earlier, although the specific mechanism cannot be isolated from the present dataset. The shaded boxes in Fig. 4 show the interquartile ranges (IQR) for each half-hour bin. During daytime, the LAS IQRs are generally wider and centered at higher values than those of EC, indicating that both greater day-to-day variability and a systematically positive offset in the LAS-derived fluxes.

The diurnal pattern revealed by the ensemble averages suggests the underlying physical mechanisms driving aerosol exchange over the inland water body. The daytime increases in aerosol fluxes indicate the dominant role of thermal

https://doi.org/10.5194/egusphere-2026-2182
Preprint. Discussion started: 19 May 2026

convection. As solar radiation heats the surface, the atmospheric stratification becomes unstable, enhancing turbulent mixing and facilitating the transport of aerosols. Conversely, the suppressed fluxes during the nighttime reflect the stabilization of
245 the boundary layer due to radiative cooling, which inhibits turbulent exchange.

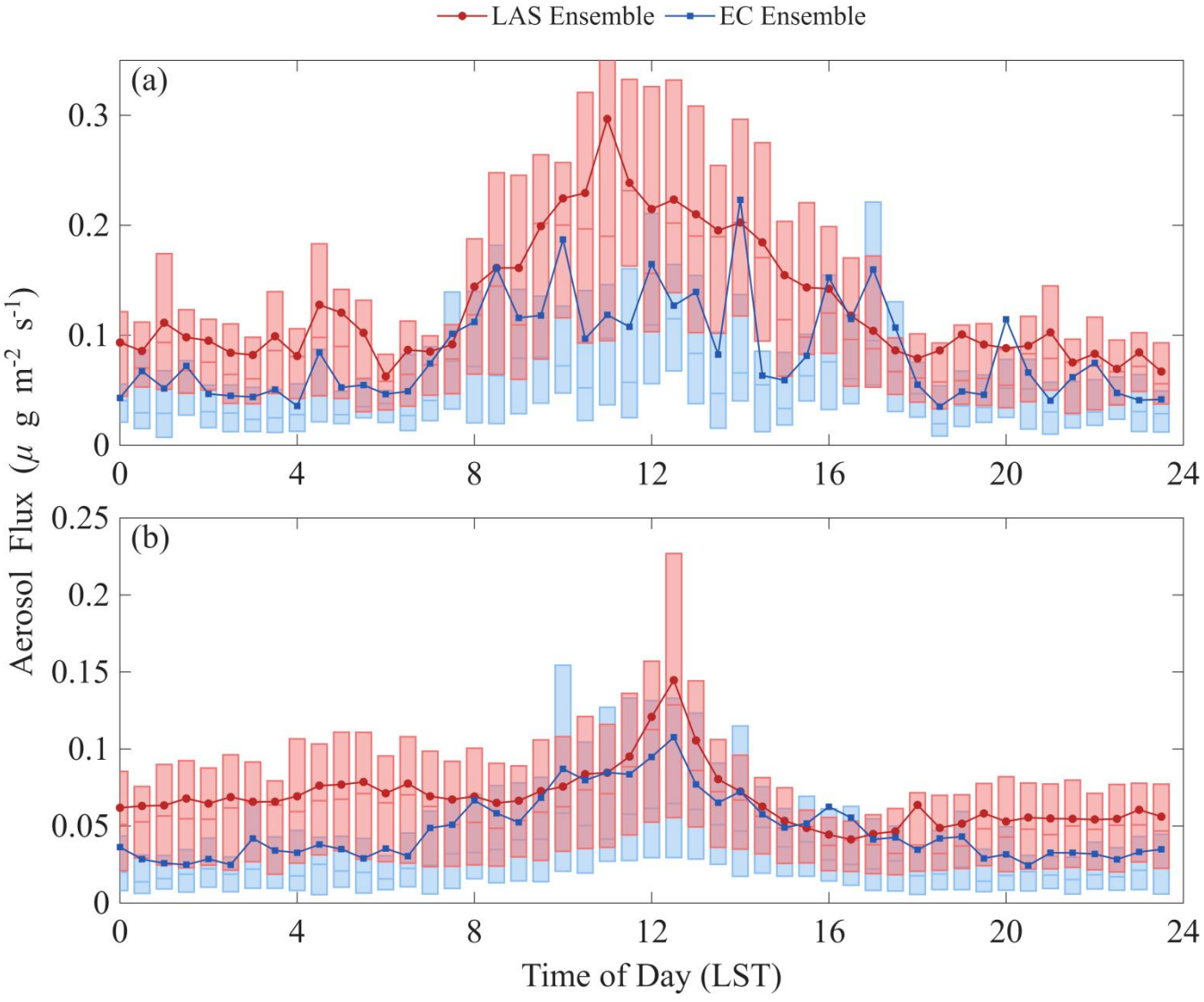

Figure 4. Ensemble diurnal variations of aerosol fluxes derived from LAS and EC measurements in **(a)** the first campaign and **(b)** the second campaign at Siyuan Lake. The solid lines with red circles and blue squares represent the ensemble mean values for LAS and EC, respectively. The shaded vertical boxes indicate the interquartile ranges of the 30-min data for each corresponding half-hour interval.

https://doi.org/10.5194/egusphere-2026-2182
Preprint. Discussion started: 19 May 2026

3.3 Comparison of LAS and EC aerosol fluxes at Sijiao Island

3.3.1 Temporal variations and footprint analysis at Sijiao Island

After the lake comparison, the analysis was extended to the coastal open-water site at Sijiao Island. Fig. 5 presents the temporal variations of aerosol fluxes derived from both methods during the two coastal campaigns. The first coastal campaign shows a markedly different behavior from the lake case (Fig. 5a). The mean fluxes were 0.168 $\mu g\ m^{-2}\ s^{-1}$ and 0.176 $\mu g\ m^{-2}\ s^{-1}$ for LAS and EC respectively, with an MBE of $-0.008\ \mu g\ m^{-2}\ s^{-1}$ and a substantially larger NRMSE of 27.9%. The slightly higher mean EC flux in this campaign is largely explained by fog events on 18 - 19 April, and early hours (00:00–02:00 LST) of 21 April, during which LAS data were missing due to optical attenuation. The fog events created extended gaps in the LAS record, whereas the EC system continued to operate and captured elevated fluxes. The exclusion of these high-value periods from the LAS series therefore biases the mean comparison for the first coastal campaign. By contrast, the second campaign was not affected by severe signal attenuation (Fig. 5b). The mean LAS and EC fluxes for were 0.091 $\mu g\ m^{-2}\ s^{-1}$ and 0.067 $\mu g\ m^{-2}\ s^{-1}$, respectively, with an MBE of 0.024 $\mu g\ m^{-2}\ s^{-1}$ and an NRMSE of 16.8%. As in the lake campaigns, LAS yields larger mean flux than EC. Overall, the coastal results suggest that LAS and EC can still track similar macroscopic temporal trends, but this agreement is clearly more robust in the second campaign than in the fog-affected first campaign.

Over the coastal environment, the observed flux variations suggest physical processes distinct from those over the inland lake, likely pointing to dynamic marine forcings. The episodic increases and sustained high values of aerosol fluxes are indicative of enhanced exchanges of marine aerosols. In the marine boundary layer, elevated wind speeds and subsequent wave breaking mechanically drive the bursting of entrained air bubbles, a well-documented source of sea spray aerosols (De Leeuw et al., 2011). Consequently, the flux variations captured by LAS at the coastal site likely reflect these wind-driven events and the active air-sea mass exchange.

A footprint analysis was used to evaluate the spatial representativeness of the two systems at the coastal site. As shown in Fig. 6, the source areas of the LAS and EC systems differ substantially in both campaigns. The EC footprint is confined to the immediate vicinity of the instrument, whereas the LAS footprint extends across the bay and integrates over a large open-water area. This mismatch is consistent with the weak first-period correlation ($r = 0.218$), as the two systems frequently sampled different source areas. Despite a similar footprint mismatch, the second coastal campaign shows a markedly higher correlation ($r = 0.612$). This improvement likely reflects the absence of severe fog attenuation and a more temporally coherent measurement period, although the specific role of surface-state homogeneity cannot be isolated here. This behavior is qualitatively consistent with previous LAS – EC comparisons for sensible heat flux studies (Li et al., 2017). More importantly, it shows that the aerosol flux comparison is strongly condition dependent, with substantially better agreement when optical attenuation is weak.

https://doi.org/10.5194/egusphere-2026-2182
Preprint. Discussion started: 19 May 2026

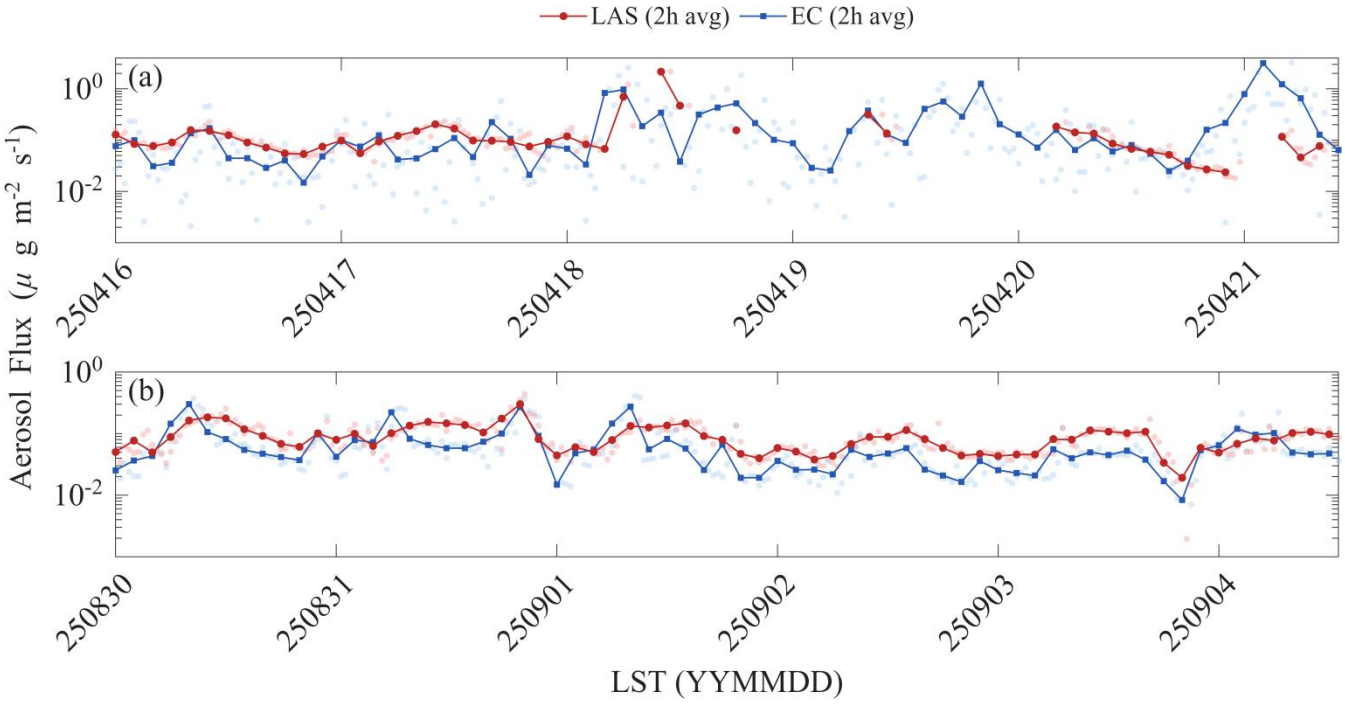

Figure 5. Temporal variations of aerosol fluxes derived from LAS and EC measurements in **(a)** the first campaign (16 to 21 April 2025) and **(b)** the second campaign (30 August to 4 September 2025) at Sijiao Island. The solid lines with red circles and blue squares denote the 2 h block averages for LAS and EC, respectively. The transparent points indicate the original data at a 30-min resolution.

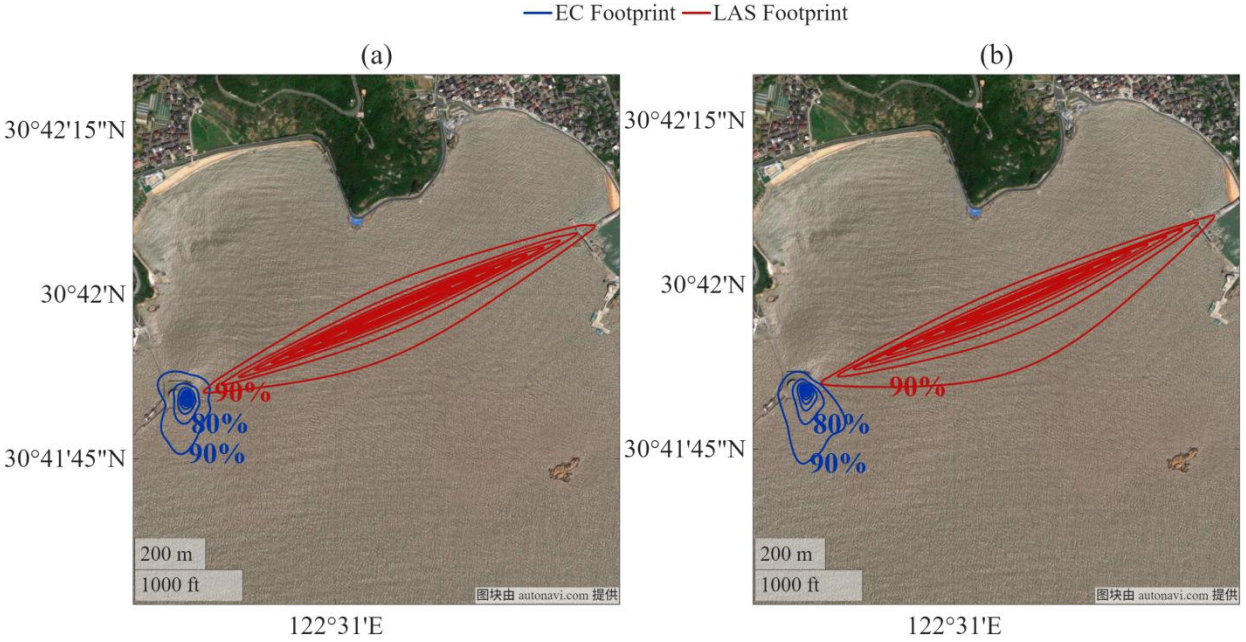

Figure 6. Spatial footprint climatology of the EC (blue solid lines) and LAS (red solid lines) systems at Sijiao Island during **(a)** the first campaign and **(b)** the second campaign. The contour lines denote the cumulative spatial contribution to the measured aerosol fluxes, representing the 10% to 90% source areas from the inside out at 10% intervals. Map tiles provided by © 2026 AutoNavi.

https://doi.org/10.5194/egusphere-2026-2182
Preprint. Discussion started: 19 May 2026

3.3.2 Ensemble diurnal cycles of aerosol fluxes at Sijiao Island

An ensemble-diurnal analysis was also applied to the coastal site. Because both coastal campaigns were short, the ensemble averages and IQRs (shaded boxes in Fig. 7) are strongly influenced by individual events and therefore should be interpreted cautiously.

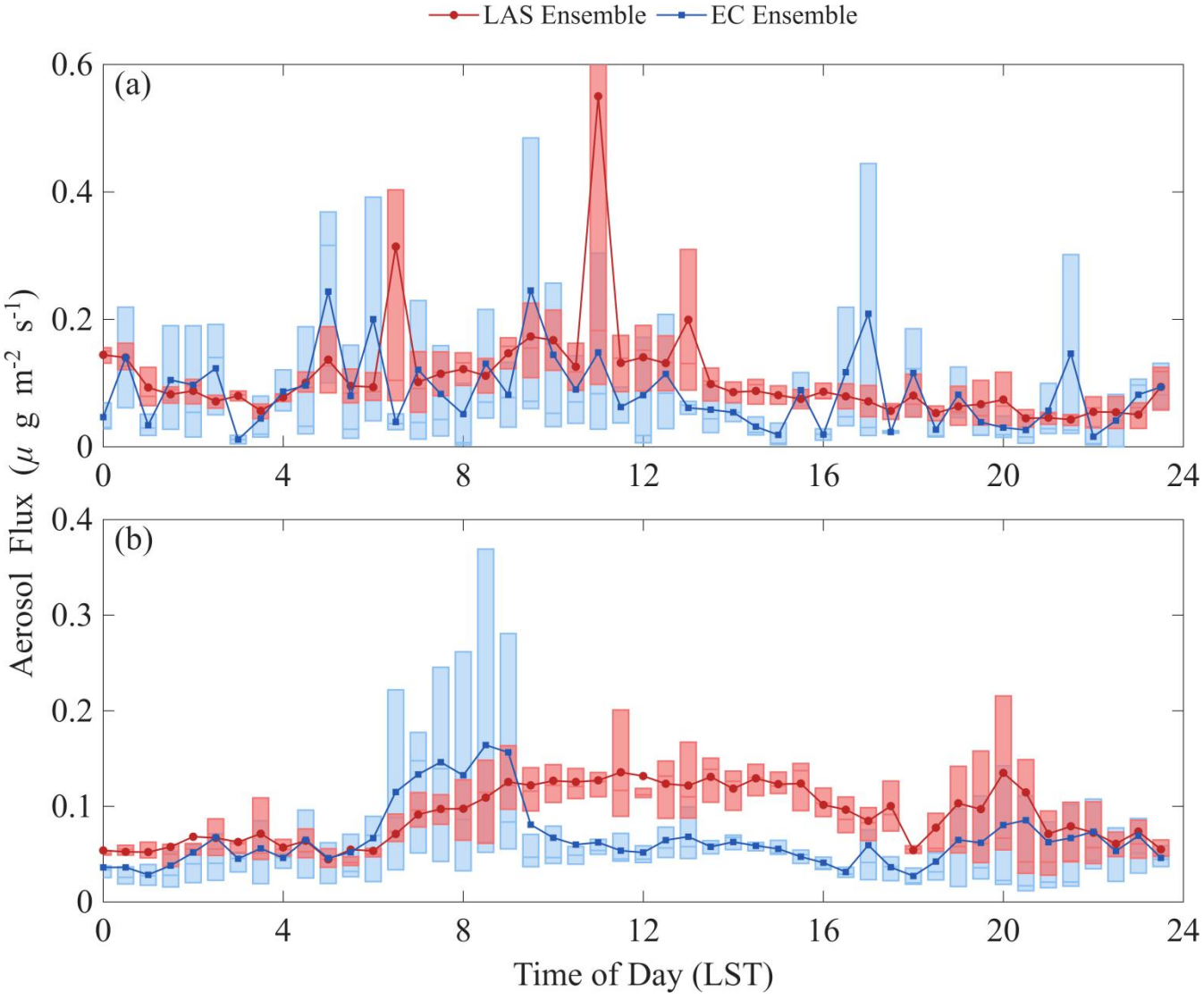

Figure 7. Ensemble diurnal variations of aerosol fluxes derived from LAS and EC measurements in **(a)** the first campaign and **(b)** the second campaign at Sijiao Island. The solid lines with red circles and blue squares represent the ensemble mean values for LAS and EC, respectively. The shaded vertical boxes indicate the interquartile ranges of the 30-min data for each corresponding half-hour interval.

In the first coastal campaign, the ensemble diurnal cycles are highly irregular and poorly synchronized (Fig. 7a). The LAS ensemble mean reveals a single sharp peak at 11:00 LST (0.550 μg m^{-2} s^{-1}), whereas the EC measurements exhibit multiple discrete and lower peaks, including 0.245 μg m^{-2} s^{-1} at 09:30 LST and 0.209 μg m^{-2} s^{-1} at 17:00 LST. The IQRs of the EC

https://doi.org/10.5194/egusphere-2026-2182
Preprint. Discussion started: 19 May 2026

system are generally wider and centered at higher values than those of LAS. This difference is largely explained by the missing LAS data during the fog-affected high-flux periods (as discussed in Sect. 3.3.1), which distort the ensemble distribution. The first-period diurnal comparison therefore should not be treated as a robust measure of method agreement.

In the second coastal campaign (Fig. 7b), the two ensemble diurnal cycles are more comparable. Both methods show higher fluxes during daytime and lower values at night. The LAS curve exhibits a broad daytime maximum from 10:00 to 15:00 LST with an average of 0.125 μg m^{-2} s^{-1}, whereas the EC series shows a distinct morning enhancement between 07:00 and 09:00 LST (averaging 0.147 μg m^{-2} s^{-1}). The IQRs indicate anomalously high values during morning periods. Field notes indicate that barbecue smoke was present near the EC installation site between 30 August and 1 September, making localized anthropogenic interference a plausible explanation for this feature. Both methods also show a small evening increase near 20:00 LST. Outside of this likely interference period, the LAS IQRs are generally wider and centered at higher values than those of EC during daytime, suggesting greater day-to-day variability and a persistent positive offset in the LAS-derived fluxes.

3.4 Comparison with independent dry-deposition calculations

To provide an additional observational constraint, the micrometeorological fluxes estimated from LAS and EC were compared with dry-deposition calculations derived from filter sampling. Because the dry- deposition calculation is not physically identical to the micrometeorological fluxes, the comparison is used here to assess broad consistency in temporal variability rather than absolute agreement.

At Siyuan Lake (Fig. 8a), both LAS and EC show similar levels of correlation with the dry-deposition calculations, with r values of 0.592 and 0.588, respectively. The mean dry-deposition flux over the lake (0.1335 μg m^{-2} s^{-1}) is substantially higher than the corresponding micrometeorological fluxes (0.0464 and 0.0416 μg m^{-2} s^{-1} for LAS and EC, respectively). Despite this difference in absolute magnitude, the similar correlation values suggest that both methods capture broadly comparable temporal variability at the lake site. The magnitude discrepancy likely reflects differences in measurement principle and in the aerosol size fractions represented by the respective approaches.

At Sijiao Island (Fig. 8b), the three mean flux estimates are of the same order of magnitude (0.1014, 0.0692, and 0.0727 μg m^{-2} s^{-1} for LAS, EC, and dry-deposition, respectively). LAS shows a somewhat higher correlation with the dry-deposition calculations ($r = 0.442$) than EC ($r = 0.346$). This result is consistent with the idea that the path-averaged LAS may better represent site-scale variability at the coastal station, but the difference is not large enough to be treated as a definitive validation of method superiority.

https://doi.org/10.5194/egusphere-2026-2182
Preprint. Discussion started: 19 May 2026

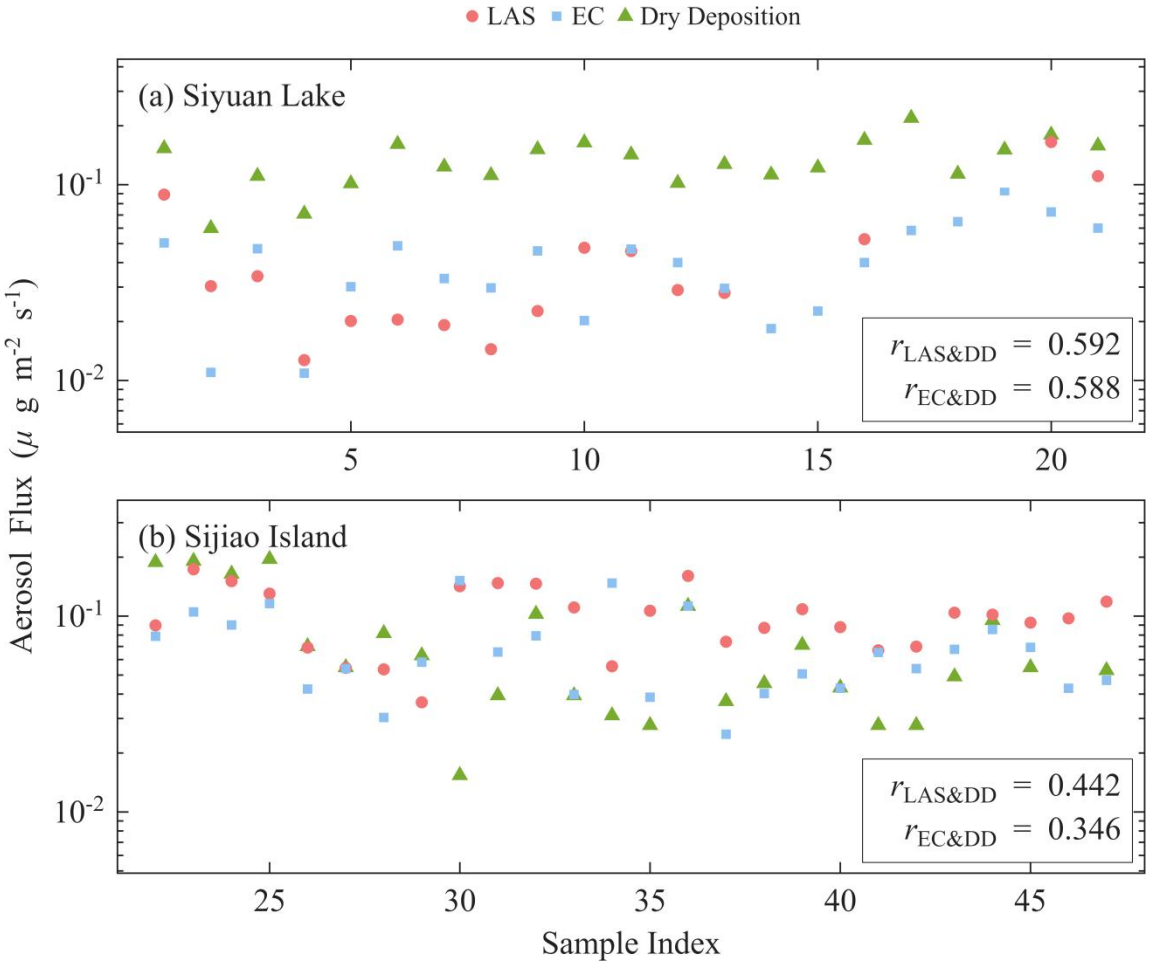

Figure 8. Comparison of aerosol fluxes derived from LAS and EC measurements against independent dry-deposition calculations at **(a)** Siyuan Lake and **(b)** Sijiao Island. The red circles, blue squares, and green triangles represent the LAS measurements, EC measurements, and dry-deposition calculations, respectively. Because the filter sampling was conducted discontinuously, the horizontal axis is represented by a sequential sample index rather than continuous time. The linear correlation coefficients (r) between the respective micrometeorological fluxes and dry-deposition calculations are annotated in the bottom right corner of each panel.

4 Conclusions

In this study, a large-aperture scintillometer (LAS) was deployed to retrieve aerosol mass fluxes over open-water environments (an inland lake and a coastal ocean) for the first time. To evaluate the applicability and operational boundaries of this optical technique, the LAS measurements were compared against conventional eddy covariance (EC) method and independent filter-based dry-deposition calculations.

Results indicate that the LAS is capable of capturing aerosol flux dynamics over water surfaces under specific conditions. During periods without severe optical attenuation, the LAS-derived fluxes exhibited consistent macroscopic temporal trends with the EC measurements, with the normalized root-mean-square error (NRMSE) constrained between 15.0% and 16.8%.

https://doi.org/10.5194/egusphere-2026-2182
Preprint. Discussion started: 19 May 2026

Because the path-averaging LAS integrates fluxes along a fixed optical line, whereas the point-measurement EC system samples a dynamic and wind-driven footprint, this fundamental difference in spatial representativeness led to footprint mismatches that likely reduced short-timescale correlations. However, ensemble diurnal analyses demonstrated that long-timescale temporal averaging bridges this spatial scale gap, improving the correlation between the two techniques.

Importantly, the coastal campaigns revealed the operational boundaries of the LAS over open-water environments. Dense fog and persistent high-humidity conditions severely attenuated the optical signal, resulting in extended data gaps during periods when the EC system remained functional. This highlights that the application of the LAS method over open water is limited by its dependence on atmospheric visibility and optical transmission.

Comparisons with independent dry-deposition calculations provided an additional observational constraint. While both techniques captured temporal variability comparably over the lake, the spatially integrated LAS fluxes maintained a higher correlation with the deposition calculations at the coastal site. Rather than demonstrating absolute methodological superiority, this result is consistent with the capacity of path-averaging scintillometers to better represent regional-scale aerosol exchange.

Ultimately, this exploratory study shows that LAS offers a spatially integrated perspective that complements traditional single-point measurements for marine aerosol research, provided that local optical boundary conditions are met.

Appendix A: Rationale for selecting a 30-min averaging period

To ensure physically representative turbulent fluxes while minimizing contamination from non-turbulent motions, an appropriate averaging period must be selected for EC calculations. In this study, we determine the averaging period using the bimodal structure of the velocity variance spectra (Liang et al 2014, Stiperski et al 2019).

The variance spectrum of velocity under non-stationary boundary-layer conditions typically exhibits two distinct energy regimes separated by a spectral gap: a high-frequency peak corresponding to turbulent eddies within the inertial subrange, and a low-frequency peak associated with mesoscale or sub-mesoscale motions. Between these two peaks, a flattened region or energy minimum is usually present, representing the scale separation where neither turbulent nor mesoscale processes dominate. Averaging times chosen within this spectral gap effectively filter out non-turbulent motions while retaining the turbulent contribution to fluxes (Barbano et al., 2022).

Figure A1 presents the pre-multiplied variance spectra of the horizontal (u, v) and vertical (w) velocity components, illustrated here using data from the first field experiment at Siyuan Lake as an example (results from the other three experiments are consistent with this case). Across all analyzed periods, the spectra display a consistent bimodal shape, with: a well-defined inertial subrange at frequencies higher than approximately 10^{-1} to 1 Hz characterized by a $-2/3$ slope, and enhanced low-frequency variance below approximately 10^{-4} Hz. Three vertical dashed lines corresponding to the commonly used averaging windows of 1 min, 5 min, and 30 min are superimposed on the variance spectra. It is evident that both the 1-min and 5-min thresholds lie close to, or partly within, the high-frequency side of the inertial subrange, indicating that turbulent eddies at these scales may still contribute energy and potentially bias the computed fluxes. In contrast, the 30-min

https://doi.org/10.5194/egusphere-2026-2182
Preprint. Discussion started: 19 May 2026

threshold is positioned entirely within the spectral-gap region, well separated from the inertial-subrange peak and well before the mesoscale energy increase. This placement confirms that the 30-min averaging window is neither affected by inertial-subrange turbulence nor influenced by mesoscale or sub-mesoscale motions, providing a reasonable separation between turbulent and non-turbulent variability.

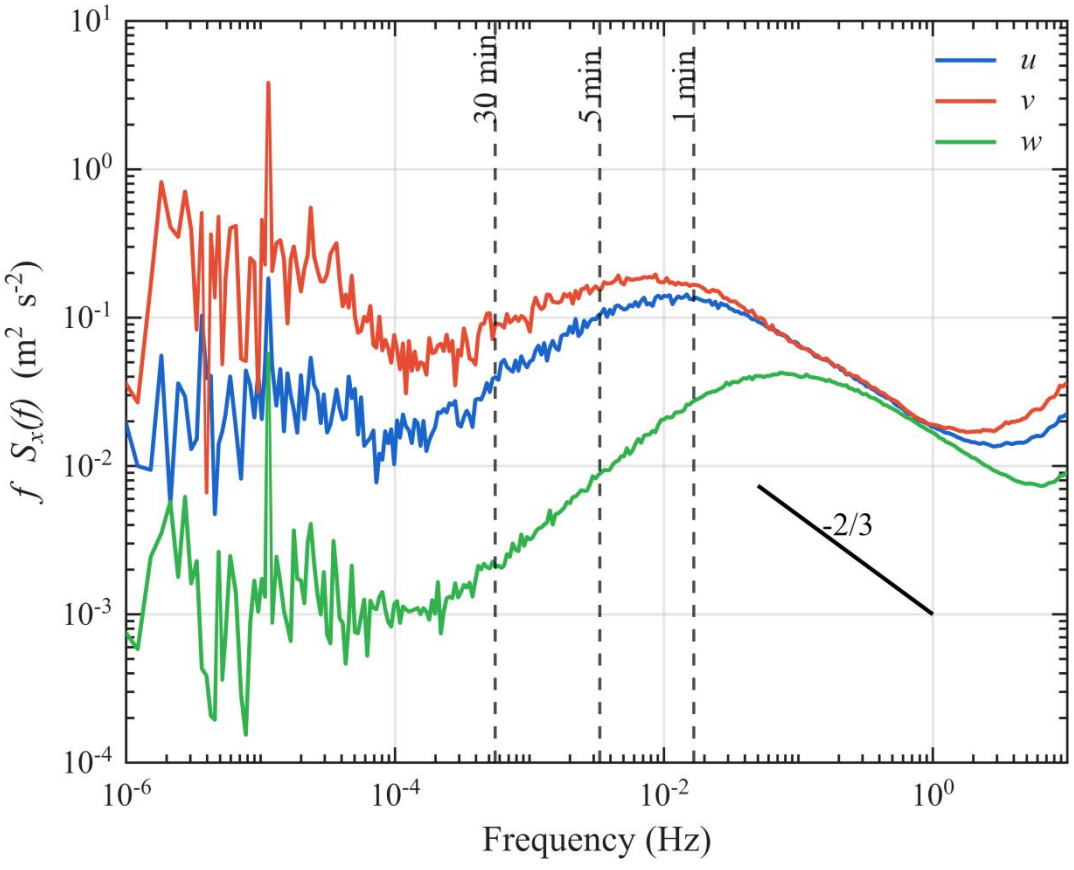

Figure A1. Pre-multiplied variance spectra of horizontal (u, v) and vertical (w) velocity components for the first experiment period at Siyuan Lake. The vertical dashed lines indicate the corresponding frequency for 30-, 5- and 1-min averaging periods from left to right. The characteristic –2/3 slope of the inertial subrange is indicated by the solid lines.

Code and data availability

The code and data used in this study are available upon request to Renjie Liu (in3.mz@sjtu.edu.cn).

Author contributions

CH, RL, and YP conceptualized the study and designed the experiments. RL and YP performed the measurements and analyzed the data. RL and YP wrote the original draft. CH was responsible for project administration and management of the

research activity planning and execution, and revised the manuscript. RY provided the methodology and reviewed the manuscript.

Competing interests

The authors declare that they have no conflict of interest.

Disclaimer

Publishers' note: Copernicus Publications remains neutral with regard to jurisdictional claims made in the text, published maps, institutional affiliations, or any other geographical representation in this paper. While Copernicus Publications makes every effort to include appropriate place names, the final responsibility lies with the authors. Views expressed in the text are those of the authors and do not necessarily reflect the views of the publisher.

Financial support

Authors acknowledge the support from the National Natural Science Foundation of China (NSFC) under Grant 42476026, the Oceanic Interdisciplinary Program of Shanghai Jiao Tong University (SL2023ZD105), Shanghai Typhoon Research Foundation (TFJJ202408), China Meteorological Administration Xiong'an Atmospheric Boundary Layer Key Laboratory (2023LABL-B18).

Review statement

The review statement will be added by Copernicus Publications listing the handling editor as well as all contributing referees according to their status anonymous or identified.

References

Andreas, E.: A review of the sea spray generation function for the open ocean, Adv. Fluid Mech., 33, 1–46, 2002.

Andreas, E. L.: A new sea spray generation function for wind speeds up to 32 m s^{-1}, J. Phys. Oceanogr., 28, 2175–2184, https://doi.org/10.1175/1520-0485(1998)028<2175:ANSSGF>2.0.CO;2, 1998.

Barbano, F., Brogno, L., Tampieri, F., and Di Sabatino, S.: Interaction between waves and turbulence within the nocturnal boundary layer, Bound.-Lay. Meteorol., 183, 35–65, https://doi.org/10.1007/s10546-021-00678-2, 2022.

Chehbouni, A., Kerr, Y., Watts, C., Hartogensis, O., Goodrich, D., Scott, R., Schieldge, J., Lee, K., Shuttleworth, W., and Dedieu, G.: Estimation of area-average sensible heat flux using a large-aperture scintillometer during the Semi-Arid

https://doi.org/10.5194/egusphere-2026-2182
Preprint. Discussion started: 19 May 2026

Land-Surface-Atmosphere (SALSA) Experiment, Water Resour. Res., 35, 2505–2511, https://doi.org/10.1029/1999WR900111, 1999.

De Bruin, H. A., Van den Hurk, B., and Kohsiek, W.: The scintillation method tested over a dry vineyard area, Bound.-Lay. Meteorol., 76, 25–40, https://doi.org/10.1007/BF00710889, 1995.

De Leeuw, G., Andreas, E. L., Anguelova, M. D., Fairall, C., Lewis, E. R., O'Dowd, C., Schulz, M., and Schwartz, S. E.: Production flux of sea spray aerosol, Rev. Geophys., 49, https://doi.org/10.1029/2010RG000349, 2011.

Ding, A., Huang, X., Nie, W., Sun, J., Kerminen, V. M., Petäjä, T., Su, H., Cheng, Y., Yang, X. Q., and Wang, M.: Enhanced haze pollution by black carbon in megacities in China, Geophys. Res. Lett., 43, 2873–2879, https://doi.org/10.1002/2016GL067745, 2016.

Fuentes, E., Coe, H., Green, D., de Leeuw, G., and McFiggans, G.: Laboratory-generated primary marine aerosol via bubble-bursting and atomization, Atmos. Meas. Tech., 3, 141–162, https://doi.org/10.5194/amt-3-141-2010, 2010.

Gaston, C. J., Cahill, J. F., Collins, D. B., Suski, K. J., Ge, J. Y., Barkley, A. E., and Prather, K. A.: The cloud nucleating properties and mixing state of marine aerosols sampled along the southern California coast, Atmosphere, 9, 52, https://doi.org/10.3390/atmos9020052, 2018.

Geever, M., O'Dowd, C. D., van Ekeren, S., Flanagan, R., Nilsson, E. D., de Leeuw, G., and Rannik, Ü.: Submicron sea spray fluxes, Geophys. Res. Lett., 32, https://doi.org/10.1029/2005GL023081, 2005.

Gong, S.: A parameterization of sea-salt aerosol source function for sub-and super-micron particles, Global Biogeochem. Cycles, 17, https://doi.org/10.1029/2003GB002079, 2003.

Hartogensis, O., Watts, C., Rodriguez, J., and De Bruin, H.: Derivation of an effective height for scintillometers: La Poza experiment in Northwest Mexico, J. Hydrometeorol., 4, 915–928, https://doi.org/10.1175/1525-7541(2003)004<0915:DOAEHF>2.0.CO;2, 2003.

Hsu, S. C., Liu, S. C., Kao, S. J., Jeng, W. L., Huang, Y. T., Tseng, C. M., Tsai, F., Tu, J. Y., and Yang, Y.: Water-soluble species in the marine aerosol from the northern South China Sea: High chloride depletion related to air pollution, J. Geophys. Res. :Atmos., 112, https://doi.org/10.1029/2007JD008844, 2007.

Huang, X. and Ding, A.: Aerosol as a critical factor causing forecast biases of air temperature in global numerical weather prediction models, Chin. Sci. Bull., 66, 1917–1924, https://doi.org/10.1016/j.scib.2021.05.009, 2021.

Huang, X., Wang, Z., and Ding, A.: Impact of aerosol-PBL interaction on haze pollution: Multiyear observational evidences in North China, Geophys. Res. Lett., 45, 8596–8603, https://doi.org/10.1029/2018GL079239, 2018.

Hultin, K. A., Nilsson, E. D., Krejci, R., Mårtensson, E. M., Ehn, M., Hagström, Å., and de Leeuw, G.: In situ laboratory sea spray production during the Marine Aerosol Production 2006 cruise on the northeastern Atlantic Ocean, J. Geophys. Res. :Atmos., 115, https://doi.org/10.1029/2009JD012522, 2010.

Kiehl, J. and Briegleb, B.: The relative roles of sulfate aerosols and greenhouse gases in climate forcing, Science, 260, 311–314, https://doi.org/10.1126/science.260.5106.311, 1993.

https://doi.org/10.5194/egusphere-2026-2182
Preprint. Discussion started: 19 May 2026

Kljun, N., Calanca, P., Rotach, M., and Schmid, H. P.: A simple two-dimensional parameterisation for Flux Footprint Prediction (FFP), Geosci. Model Dev., 8, 3695–3713, https://doi.org/10.5194/gmd-8-3695-2015, 2015.

Lana, A., Bell, T., Simó, R., Vallina, S. M., Ballabrera-Poy, J., Kettle, A., Dachs, J., Bopp, L., Saltzman, E., and Stefels, J.: An updated climatology of surface dimethlysulfide concentrations and emission fluxes in the global ocean, Global Biogeochem. Cycles, 25, https://doi.org/10.1029/2010GB003850, 2011.

Laskin, A., Moffet, R. C., Gilles, M. K., Fast, J. D., Zaveri, R. A., Wang, B., Nigge, P., and Shutthanandan, J.: Tropospheric chemistry of internally mixed sea salt and organic particles: Surprising reactivity of NaCl with weak organic acids, J. Geophys. Res. :Atmos., 117, https://doi.org/10.1029/2012JD017743, 2012.

Lewis, E. R. and Schwartz, S. E.: Sea salt aerosol production: mechanisms, methods, measurements, and models, American geophysical union, https://doi.org/10.1029/GM152, 2004.

Li, Q., Zhang, H., Cai, X., Song, Y., and Zhu, T.: The impacts of the atmospheric boundary layer on regional haze in North China, npj Clim. Atmos. Sci., 4, 9, https://doi.org/10.1038/s41612-021-00165-y, 2021.

Li, X., Gao, Z., Li, Y., and Tong, B.: Comparison of sensible heat fluxes measured by a large aperture scintillometer and eddy covariance system over a heterogeneous farmland in East China, Atmosphere, 8, 101, https://doi.org/10.3390/atmos8060101, 2017.

Liang, J., Zhang, L., Wang, Y., Cao, X., Zhang, Q., Wang, H., and Zhang, B.: Turbulence regimes and the validity of similarity theory in the stable boundary layer over complex terrain of the Loess Plateau, China, J. Geophys. Res. :Atmos., 119, 6009–6021, https://doi.org/10.1002/2014JD021510, 2014.

Meijninger, W., Hartogensis, O., Kohsiek, W., Hoedjes, J., Zuurbier, R., and De Bruin, H.: Determination of area-averaged sensible heat fluxes with a large aperture scintillometer over a heterogeneous surface–Flevoland field experiment, Bound.-Lay. Meteorol., 105, 37–62, https://doi.org/10.1023/A:1019647732027, 2002.

Monahan, E., Spiel, D., and Davidson, K.: A model of marine aerosol generation via whitecaps and wave disruption, in: Oceanic whitecaps: And their role in air-sea exchange processes, Springer, 167–174, https://doi.org/10.1007/978-94-009-4668-2_16, 1986.

Norris, S., Brooks, I., de Leeuw, G., Smith, M., Moerman, M., and Lingard, J.: Eddy covariance measurements of sea spray particles over the Atlantic Ocean, Atmos. Chem. Phys., 8, 555–563, https://doi.org/10.5194/acp-8-555-2008, 2008.

Ovadnevaite, J., Manders, A., De Leeuw, G., Ceburnis, D., Monahan, C., Partanen, A.-I., Korhonen, H., and O'dowd, C.: A sea spray aerosol flux parameterization encapsulating wave state, Atmos. Chem. Phys., 14, 1837–1852, https://doi.org/10.5194/acp-14-1837-2014, 2014.

Petroff, A. and Zhang, L.: Development and validation of a size-resolved particle dry deposition scheme for application in aerosol transport models, Geosci. Model Dev., 3, 753–769, https://doi.org/10.5194/gmd-3-753-2010, 2010.

Revell, L. E., Kremser, S., Hartery, S., Harvey, M., Mulcahy, J. P., Williams, J., Morgenstern, O., McDonald, A. J., Varma, V., and Bird, L.: The sensitivity of Southern Ocean aerosols and cloud microphysics to sea spray and sulfate aerosol

https://doi.org/10.5194/egusphere-2026-2182
Preprint. Discussion started: 19 May 2026

production in the HadGEM3-GA7. 1 chemistry–climate model, Atmos. Chem. Phys., 19, 15447–15466, https://doi.org/10.5194/acp-19-15447-2019, 2019.

Salter, M. E., Zieger, P., Acosta Navarro, J. C., Grythe, H., Kirkevåg, A., Rosati, B., Riipinen, I., and Nilsson, E. D.: An empirically derived inorganic sea spray source function incorporating sea surface temperature, Atmos. Chem. Phys., 15, 11047–11066, https://doi.org/10.5194/acp-15-11047-2015, 2015.

Sasakawa, M., Ooki, A., and Uematsu, M.: Aerosol size distribution during sea fog and its scavenge process of chemical substances over the northwestern North Pacific, J. Geophys. Res. :Atmos., 108, https://doi.org/10.1029/2002JD002329, 2003.

Seinfeld, J. H., Bretherton, C., Carslaw, K. S., Coe, H., DeMott, P. J., Dunlea, E. J., Feingold, G., Ghan, S., Guenther, A. B., and Kahn, R.: Improving our fundamental understanding of the role of aerosol− cloud interactions in the climate system, Proc. Natl. Acad. Sci. U.S.A., 113, 5781–5790, https://doi.org/10.1073/pnas.1514043113, 2016.

Slinn, W., Hasse, L., Hicks, B., Hogan, A., Lal, D., Liss, P., Munnich, K., Sehmel, G., and Vittori, O.: Some aspects of the transfer of atmospheric trace constituents past the air-sea interface, Atmos. Environ. (1967), 12, 2055–2087, https://doi.org/10.1016/0004-6981(78)90163-4, 1978.

Stiperski, I., Calaf, M., and Rotach, M. W.: Scaling, anisotropy, and complexity in near-surface atmospheric turbulence, J. Geophys. Res. :Atmos., 124, 1428–1448, https://doi.org/10.1029/2018JD029383, 2019.

Tatarski, V. I.: Wave propagation in a turbulent medium, McGraw-Hill Book Company Inc., New York, 285 pp., https://doi.org/10.1063/1.3057286, 1961.

Twomey, S.: The influence of pollution on the shortwave albedo of clouds, J. atmos. Sci, 34, 1149–1152, https://doi.org/10.1175/1520-0469(1977)034<1149:TIOPOT>2.0.CO;2, 1977.

van de Hulst, H. C. : Light scattering by small particles, John Wiley & Sons, Inc., New York, Library of Congress Catalog Card Nuember 57-5936, 470pp., 1957.

Ward, H., Evans, J. G., and Grimmond, C. S. B.: Multi-scale sensible heat fluxes in the suburban environment from large-aperture scintillometry and eddy covariance, Bound.-Lay. Meteorol., 152, 65–89, https://doi.org/10.1007/s10546-014-9916-4, 2014.

Wilczak, J. M., Oncley, S. P., and Stage, S. A.: Sonic anemometer tilt correction algorithms, Bound.-Lay. Meteorol., 99, 127–150, https://doi.org/10.1023/A:1018966204465, 2001.

Yang, M., Bell, T. G., Hopkins, F. E., and Smyth, T. J.: Attribution of atmospheric sulfur dioxide over the English Channel to dimethyl sulfide and changing ship emissions, Atmos. Chem. Phys., 16, 4771–4783, https://doi.org/10.5194/acp-16-4771-2016, 2016.

Yuan, R., Luo, T., Sun, J., Zeng, Z., Ge, C., and Fu, Y.: A new method for measuring the imaginary part of the atmospheric refractive index structure parameter in the urban surface layer, Atmos. Chem. Phys., 15, 2521–2531, https://doi.org/10.5194/acp-15-2521-2015, 2015.

https://doi.org/10.5194/egusphere-2026-2182
Preprint. Discussion started: 19 May 2026

Yuan, R., Luo, T., Sun, J., Liu, H., Fu, Y., and Wang, Z.: A new method for estimating aerosol mass flux in the urban surface layer using LAS technology, Atmos. Meas. Tech., 9, 1925–1937, https://doi.org/10.5194/amt-9-1925-2016, 2016.

Yuan, R., Zhang, X., Liu, H., Gui, Y., Shao, B., Tao, X., Wang, Y., Zhong, J., Li, Y., and Gao, Z.: Aerosol vertical mass flux measurements during heavy aerosol pollution episodes at a rural site and an urban site in the Beijing area of the North China Plain, Atmos. Chem. Phys., 19, 12857–12874, https://doi.org/10.5194/acp-19-12857-2019, 2019.

Yuan, R., Shi, C., Liu, H., Wang, Y., Qiao, B., and Wang, Z.: A method for estimating the ratio of aerosol mass concentration to the imaginary part of the atmospheric complex refractive index and its application, Atmos. Res., 264, 105848, https://doi.org/10.1016/j.atmosres.2021.105848, 2021.

Yuan, R., Zhang, H., Hua, J., Liu, H., Wu, P., Zhu, X., and Sun, J.: Comparison of the imaginary parts of the atmospheric refractive index structure parameter and aerosol flux based on different measurement methods, Atmos. Meas. Tech., 17, 2089–2102, https://doi.org/10.5194/amt-17-2089-2024, 2024.

Zábori, J., Krejci, R., Ström, J., Vaattovaara, P., Ekman, A., Salter, M., Mårtensson, E., and Nilsson, E.: Comparison between summertime and wintertime Arctic Ocean primary marine aerosol properties, Atmos. Chem. Phys., 13, 4783–4799, https://doi.org/10.5194/acp-13-4783-2013, 2013.

Zinke, J., Nilsson, E. D., Markuszewski, P., Zieger, P., Mårtensson, E. M., Rutgersson, A., Nilsson, E., and Salter, M. E.: Sea spray emissions from the Baltic Sea: comparison of aerosol eddy covariance fluxes and chamber-simulated sea spray emissions, Atmos. Chem. Phys., 24, 1895–1918, https://doi.org/10.5194/acp-24-1895-2024, 2024.